The Reflection Grating Spectrometer on board XMM

A. Brinkman, H. Aarts, A. den Boggende, T. Bootsma, L. Dubbeldam, J. den Herder, J. Kaastra, P. de Korte, B. van Leeuwen, R. Mewe, F. Paerels, C. de Vries

Space Research Organisation the Netherlands, Sorbonnelaan 2, 3584 CA Utrecht, The Netherlands

J. Cottam, T. Decker, S. Kahn, A. Rasmussen, J. Spodek

Columbia Astrophysics Laboratory, Columbia University, 538 West 120th Street, New York, NY 10027, USA

G. Branduardi-Raymont, P. Guttridge

Mullard Space Science Laboratory, Holmbury St. Mary, Dorking, Surrey, RH5 6NT, UK

K. Thomsen, A. Zehnder, M. Guedel

Paul Scherrer Institute, CH-5232 Villigen, Switzerland

ABSTRACT

The Reflection Grating Spectrometer (RGS) consists of an array of flat reflection gratings, positioned behind the telescope and a CCD based detector system in the spectroscopic focus. There are two identical RGS-instruments, behind two of the three telescopes. Roughly half of the X-ray light of the telescope beam is utilized by the spectrometer, the other half is focussed on the EPIC detector in the mirror focus. The first order spectral bandpass runs from 5 to 35 Å (2.5 keV - 0.35 keV). The spectral resolving power ranges from about 150 till 800 (in the first spectral order). The intrinsic energy resolution of the CCD detector is used to separate the overlapping spectral orders.

The two integrated systems, telescope, grating array and detector have been tested in a long beam X-ray test-facility (Panter facility in Munich). Results of the calibration regarding effective area and spectral resolution of the different orders will be discussed.

1. Introduction

While discussing the spectroscopic capabilities of the Reflection Grating Spectrometer (RGS) on board XMM, it is important to recognize the spectroscopic capabilities of the total integrated payload, because the three instruments, EPIC, RGS and OM are co-aligned in the spacecraft and will always be observing simultaneously. Per observation the payload offers; broadband 0.2-10 keV spectroscopy with a resolving power $E/\Delta E$ (FWHM) of between 5 and 60 with EPIC, high resolution spectroscopy between 5-35 Å(2.5-0.35 keV) with a resolving power of about 400 at 0.5 keV with RGS, and optical monitoring between 1700 and 6000 Å to a limiting magnitude of 24 over part of the wavelength band with the OM.

The 0.2-10 keV energy band contains the K-shell transitions of carbon, oxygen, neon, magnesium, aluminium, silicon, sulphur and calcium as well as both the L– and K–shell transitions of iron. Of particular interest, due to their high abundances, are oxygen and iron at temperatures of 10^6 K and 10^7-10^8 K, respectively. Detailed analysis of these spectral features will permit the determination of the physical characteristics (density, temperature, ionization state, element abundances, mass motions, deviations from Maxwellian distributions and redshift) of the emitting region and its surrounding environment. The spectral properties of a gaseous medium will depend on whether the ionization process is caused by electron colisions (a thermal model) or by photo-ionization (a nebular model), on whether the plasma is in a transient or steady state, and on whether the plasma is optically thin or optically thick.

The key parameters in the design of the spectrometer are the spectral range, the spectral resolution and the sensitivity. The spectral range selected for RGS (5-35 Å) contains most of the above mentioned K-shell transitions, with the notable exception of Fe-K, and contains the important L-shell transitions of Fe. The specification on the resolving power stems from the requirement to be able to resolve the He-like triplets of the most abundant elements in the spectral band (line ratios of triplets are important plasma diagnostic tools). Finally the grating reflection efficiency has been optimized for the Fe-L line energy range ($\sim$ 1 keV).

With present-day technology, high resolution X-ray spectroscopy in the low energy band can only be achieved with dispersive optical systems. Even the best available non-dispersive spectrometers cannot yield adequate resolution at energies below about 1 keV. Since spectral resolution degrades linearly with the angular resolution of the focussing optics, however, the moderate resolution of the XMM telescopes imposes severe constraints on the design of potential dispersive spectrometers. For the transmission gratings, which have been incorporated in Einstein and Exosat and will be used on AXAF, this requires very high line densities, which cannot be fabricated with existing technology. Reflection gratings in contrast, offer the possibility of very high dispersion with modest line densities ($\leq$ 1000 lines/mm). With proper optimization of the grating parameters, they can also yield high diffraction efficiency in the desired spectral band.

2. Instrument concept, optical design

The RGS design incorporates an array of reflection gratings placed in the converging beam at the exit from the X-ray telescope. The grating stack picks off roughly half of the X-ray light and deflects it to a strip of CCD detectors offset from the telescope focal plane. The remaining light passes undeflected through the grating stack where it is utilized by EPIC in the telescope focal plane. Nine large format back–illuminated CCDs will be operated in single photon counting and frame transfer mode at a temperature of minus $80°C$. For each photon, the position and the energy will be measured; the position to determine the high resolution X-ray spectrum as diffracted by the grating module, and the energy and position to separate out the contributions from the various overlapping grating orders, the inflight calibration source and to reduce the background.

The RGA contains 182 identical gratings. The gratings are mounted at grazing incidence to the beam in the inplane or classical configuration, in which the incident and diffracted rays lie in a plane which is perpendicular to the grating grooves. Because the beam is converging, the gratings are not parallel, they are oriented so that the graze angle of the incident ray which intercepts the center of the grating, α, is the same for all gratings in the array. In addition, the gratings are mounted so that their centers lie on a Rowland circle which also contains the telescope focus and the spectral detector (see Figure 1). In this configuration, aberrations which would otherwise be introduced by the arraying geometry, are eliminated. To fill out the array, the plane of the Rowland circle rotates about an axis passing through the telescope focus and the first order blaze focus. At any given position the grating grooves are nearly perpendicular to this plane. So as to make the array contiguous, the gratings are therefore slightly trapezoidal with their long edges parallel to the local converging light. In addition the groove density on the gratings is not constant across the grating surface. This is because the incident beam is converging, and aberrations would result if the line density were held fixed. The dimensions of the RFC detector strip and the locations of various wavelengths along this strip are indicated on Figure 1.

The dispersion equation for the spectrometer is given by $m\lambda = d(\cos\beta - \cos\alpha)$ where m is the spectral order, d is the groove spacing, β is the angle between the outgoing ray and the grating plane, and α is the angle between the incoming ray and the grating plane referred to above. The gratings are fabricated to have 'blazed' groove profiles, as shown in Figure 1 where the facets are all tilted at an angle, δ, relative to the grating plane. With the orientation shown, the light is primarily diffracted into the 'inside' spectral orders, where $m < 0$, so that $\beta > \alpha$. The diffraction efficiency is maximized when the incident and exit angles on the facets are equal. Because the outgoing rays reflect at larger angles than the incoming rays, neighboring gratings within the array vignet part of the diffracted light. The separation between the gratings is chosen to be as close as possible without vignetting the blaze wavelength. This implies that only a fraction of the light exiting the telescope is intercepted by the RGA. With the criterion above, this fraction, η, is given approximately by: $\eta = \sin\alpha / \sin\beta_{\rm blaze} = 0.53$ (ignoring obstruction by structural elements). (see also Brinkman et al 1996)

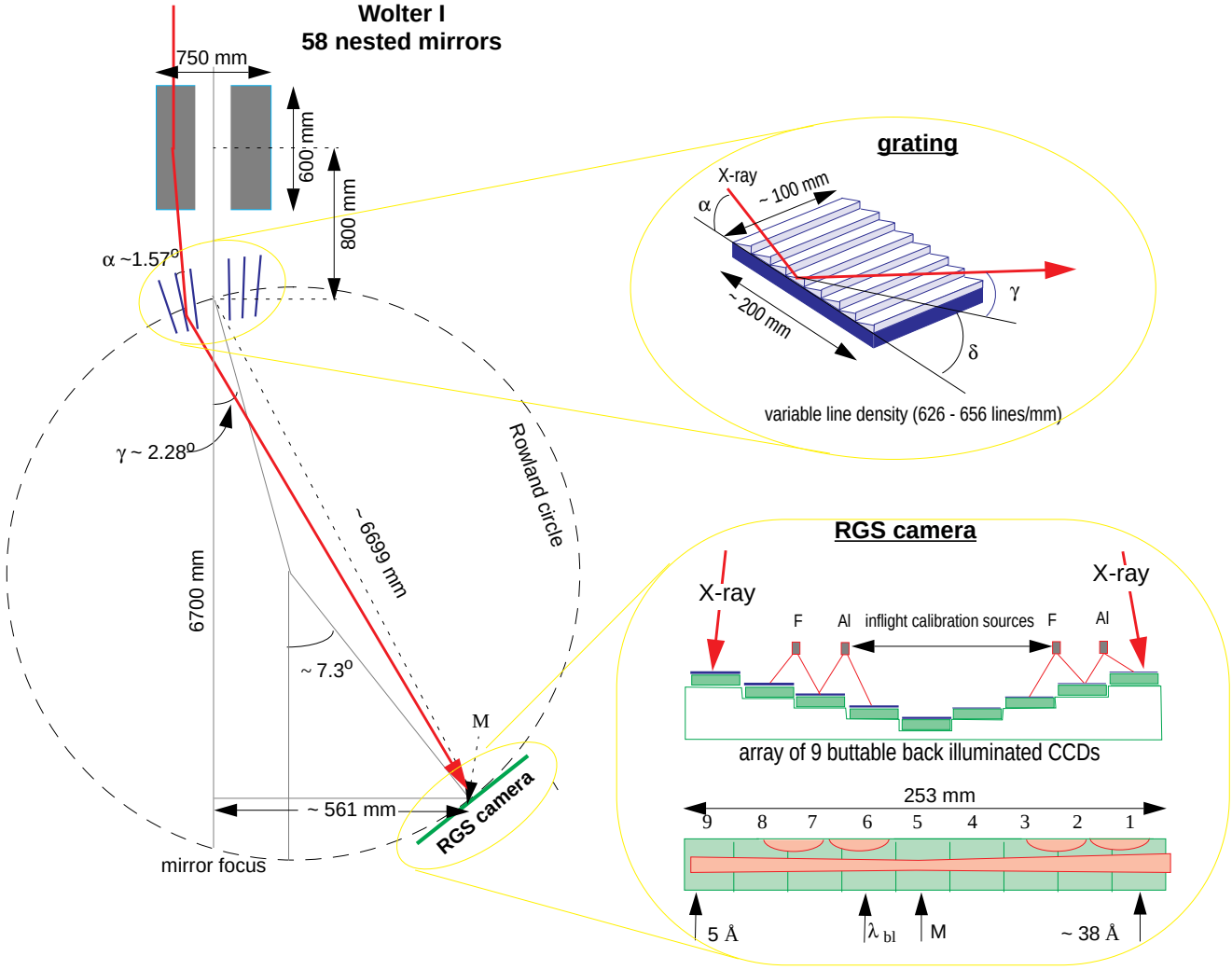

Fig. 1.— Schematic lay-out of the RGS instrument.

3. Instrument Description

3.1. Reflection Grating Array

The reflection grating array (RGA) contains 182[1] identical diffraction gratings, each measuring about 10 by 20 cm. The gratings are mounted at grazing incidence to the incident beam. The large grating substrates must be made very thin in order to keep the obstruction of the beam by the grating edges within reasonable limits. Early in the programme Beryllium was selected as the substrate material because of strength and mass considerations. However, it turned out to be very difficult to make Be-substrates with the required flatness tolerance. The actual substrate material now is SiC. The substrates are 1 mm thick with five stiffening ribs at the back running in the direction of the X-ray beam in order to maintain the required shape. The face sheets are fabricated to 1 λ (634.8 nm) and 10 λ flatness in the long and short direction, respectively.

The gratings are replicated from an identical set of master gratings onto the thin substrates. Master- gratings produced by both mechanical ruling and by holographic means have been tested and evaluated in this programme. Although holographic masters have been produced with somewhat higher reflection efficiency and lower scattering than mechanically ruled masters, unfortunately no suitable variable line density holographic master was available at the time of the flight model production.

The grating array support structure has been machined out of a monolithic billet of vacuum hot-pressed Beryllium. Due to the importance of minimizing residual stress in the grating support structure, electrical discharge machining (spark erosion) is used in the initial machining process. Figure 2 shows the integrated grating array. The Be-structure, the grating plates with the ribs clearly visible and the Ti-flexible mounts are identified.

The precision alignment of the grating array is achieved by positioning the individual gratings against four, coplanar bosses which are precision-machined into stainless steel alignment rails mounted to the beryllium support structure. The gratings are held in this position by sets of spring chips. Alignment of the rails is achieved by interferometrically measuring the orientation and flatness of the first grating inserted for each set of rails. The array is supported from an attachment ring at the mirror assembly by three kinematic, titanium flexures. For a more detailed description see Kahn et al (1996).

---

[1] The original design contained 202 identical gratings. During vibration tests of a flight representative model, it appeared that the Be-structure needed further stiffening in order to maintain positional stability of the gratings. This resulted in replacing 20 gratings by stiffening structures (braces)

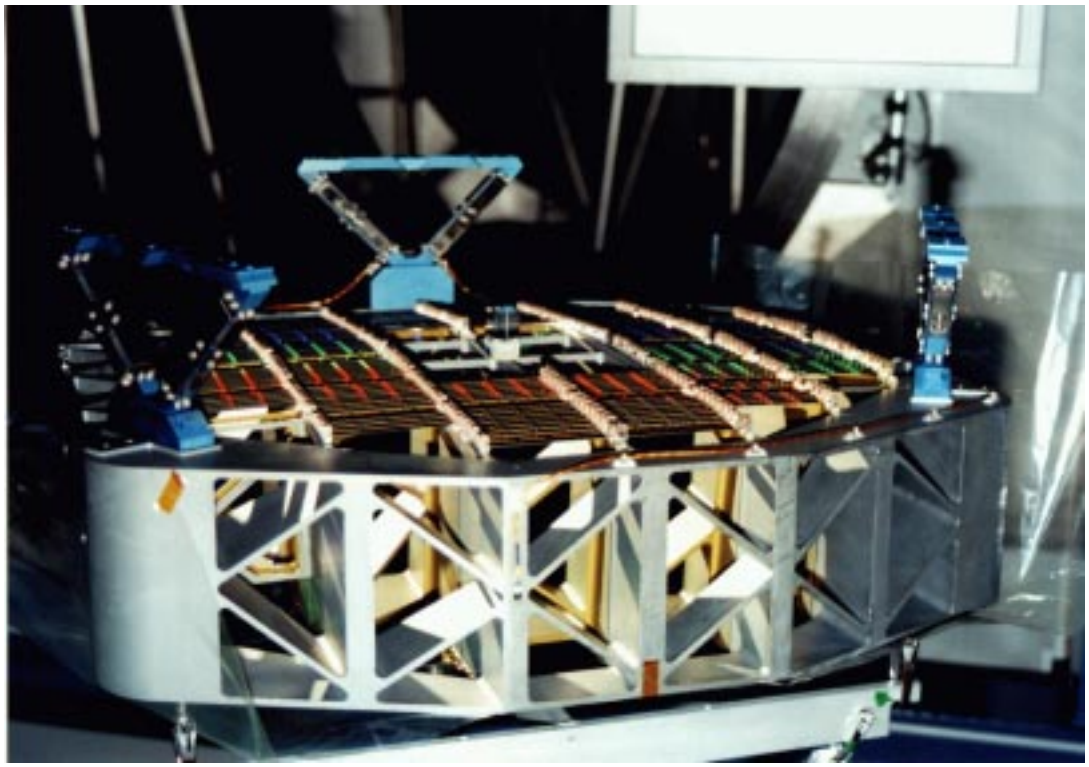

Fig. 2.— Reflection Grating Array.

3.2. Focal Plane Assembly

Thermal requirements are an important driver for the design of the focal plane camera. Three thermal nested shells constitute the interior of the camera; the CCD bench, heatshield 1 and heatshield 2. The CCD bench in the center contains nine CCDs mounted in a row, following the curvature along the Rowland circle. The bottom of the CCD bench interfaces to a coldfinger which provides the necessary cooling and ensures a uniform temperature of the bench on which the CCDs are mounted. A cover closes the CCD bench, and provides some reinforcement of the total stiffness of that assembly while leaving only an entrance slit open for incoming X-rays. For radiation shielding purposes as well as for sufficient heat conduction along the bench, a rather massive wall thickness around the CCDs is provided. Figure 3a shows a cross section of the focal camera unit, figure 3b shows a picture of one of the two flight cameras.

In order to optimize weight and stiffness, some of the needed shielding mass is incorporated in the shape of the first heatshield which encloses the CCD bench. A second, outer heatshield serves mainly for thermal purposes and is therefore made of thinner aluminium. This outer heatshield

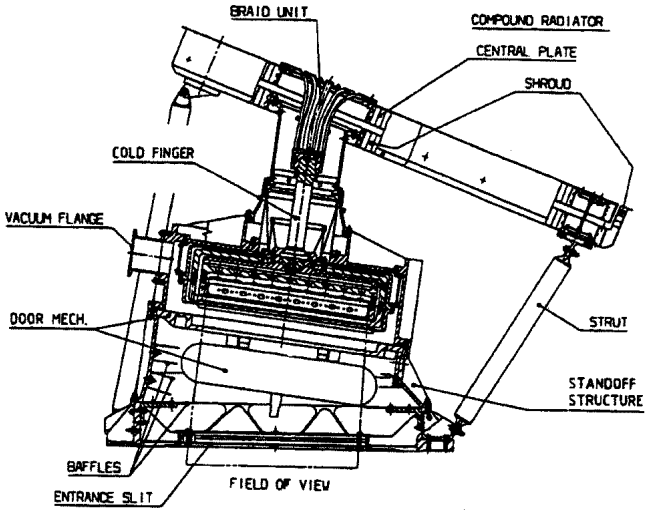

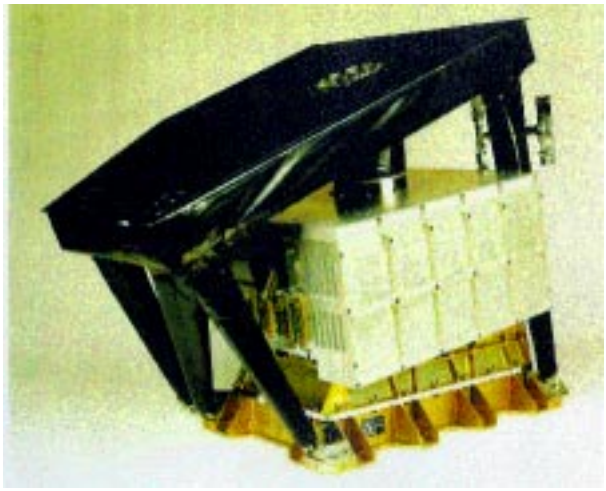

Fig. 3.— Sketch and picture of one RGS focal plane camera.

is mounted on delrin standoffs on the detector housing while CCD bench and inner heatshield are supported by a 'labyrinth' structure. This central structural element in the focal camera unit meets conflicting mechanical and thermal requirements: while providing a firm and exact position for the CCDs, heat losses due to conductive coupling between the cold interior and the detector box and the warm outside have to be minimized. This is accomplished by extending the length of the heat path and by selecting a thermally low conducting structural material (titanium alloy). The inner heatshield sits directly on the labyrinth. The CCD bench bottom plate is only indirectly mounted to this structure. In its center the labyrinth has a hole where a coldfinger passes through. An un-interrupted heatflow between the heatsink, i.e. radiator, on one end and the CCD bench on the other is necessary in order to avoid substantial temperature drops over this path and thus to arrive at the lowest envisaged temperatures on the CCD bench. For this purpose special

care has been put in the design of the interface coldfinger-CCD bench and coldfinger labyrinth, respectively. In the first case it is essential to guarantee the best possible contact at the lowest temperatures whereas the second interface poses a high thermal impedance when the CCDs have to be cold. Both issues are addressed with clamps that can be regarded as a somewhat variable thermal contact due to changes in clamping force. This change in contact pressure derives from the difference in the coefficient of thermal linear expansion between aluminium versus steel and titanium, respectively (Thomsen and Heidenreich 1994). The radiator (Thomsen 1991) is a two stage design, which will allow the CCDs to be operated as low as $-120°C$, whereas the normal operating temperature is $-80°C$.

Figure 3a also shows the door, covering the entrance slit to the interior. The door will always be closed on ground to assure a clean environment for the CCDs and will only be opened for RGS system X-ray testing. For that purpose a non-flying motor drive is attached which can open and close the door. In orbit the door can be opened only once. In order to maintain vacuum in the camera head, or keep the interior filled with dry gas, under test and storage conditions on the ground, a vacuum tube with a manual valve has been incorporated.

The focal camera unit also contains the CCD-dedicated, front end electronics which drives the CCDs and provides the CCDs output signals.

The detector is configured as a strip detector along the Rowland circle with a radius of 335 cm. In order to cover the 5-35 Å range, a length of 253 mm is required. The nine CCD-chips are back–illuminated GEC/EEV devices with 2 x 384 by 1024 pixels, of 27 x 27 μm^2 each (Bootsma et al (1996); Van den Berg et al 1996). The width of the detector is matched to the height of the RGS spectrum (2.2 mm for 90 % energy width) and to the spacecraft absolute pointing error. For optimum scientific performance, we operate the detector in the so–called frame transfer mode: the image is first accumulated in one half of the CCD (image section) and then quickly transferred to the other half (storage section) prior to read–out. Because of this quick transfer, data are not smeared out during the read–out as it is the case in a 'full area imaging mode'. Operating in the full area image mode in our design would result in a smear–out of about 10 % of the data, since the nine CCDs are read–out sequentially.

The 1024 pixel serial output has been equiped with two low noise on–chip amplifiers, which by separation of the gate structure of this register into two parts, can be used simultaneously. This doubles the read–out speed and gives redundancy in case of an amplifier failure. The lay–out of the chips is shown in Figure 4.

Figure 5 shows the schematic diagram of a cross section through a back-illuminated CCD. Diffusion of the primary electron cloud, during its transport (drift) from the X-ray absorbtion position to the bottom of the potential well, generates split events, events in which the charge created by one X-ray photon is spread out over two or more pixels. Without additional split event processing, either on board or on the ground, the existence of split events would give rise to efficiency loss at the low energy side of the spectrometer, degraded energy resolution and an

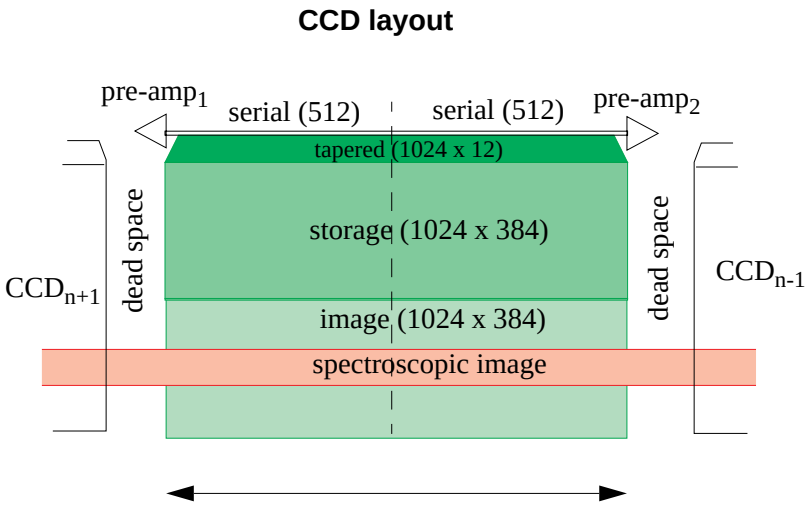

Fig. 4.— CCD lay-out.

increased background due to the need for wider energy band thresholds. Split event handling can be performed in two different ways, by on-chip binning and by split event processing. The resolution elements of the RGS 0.25 x 2.0 mm, are of course very much oversampled by the CCD pixelsize of 27 μm square. On-chip (noise free) binning of up to 3 x 3 pixels is possible without any penalty to the spectral resolution of the RGS and is therefore the baseline. The curve indicates the variation of the potential within the CCD.

The noise of a CCD, usually expressed in the number of r.m.s. electrons/pixel, is due to read-out noise and dark current noise. The read-out noise component is governed by the noise of the on-chip amplifier and the bandwidth of the electronics.

The dark current contribution to the noise is a function of temperature and of charge sampling time. From the technical point of view we want to operate the detector at the highest possible temperature, minimizing the problems with detector contamination.

The background rejection for the RGS CCDs can be performed by the use of energy discrimination. The remaining background is then subsequently rejected on the ground by the energy windows set as a function of position and grating order.

Since CCDs have high efficiency for detection of optical light we have included a filter for the rejection of optical photons. The filter analysis has been performed taking into account the diffuse sky component and bright stars. The calculated efficiency, including the different filter components, and a few calibration points, is given in Figure 6. Depending on the position in the array, the CCDs have been covered with a layer of Al with a thickness of 450, 680 or 750 Å.

For the detector calibration/monitoring, a fluorescence X-ray source has been incorporated.

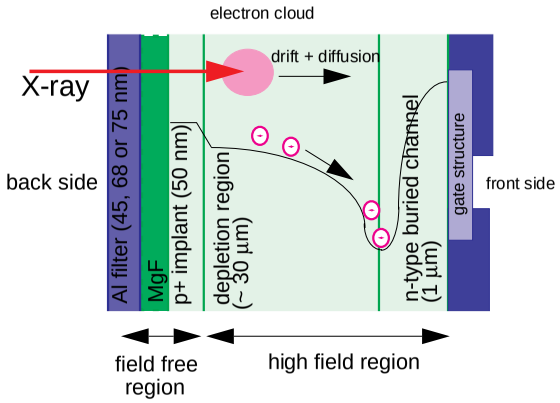

Fig. 5.— Cross section through back–illuminated RGS–CCD.

As the primary source we will utilize an α-emitter, ^{244}Cm, to bombard a target. By selecting the proper target material one can generate fluorescence X-ray lines in the energy range of the instrument. For RGS, we selected Aluminium and teflon as target materials, producing lines of Aluminium and Fluorine, respectively. The use of the sources is twofold, not only will it allow energy gain monitoring, but also monitoring of the efficiency variation with time. The latter is particularly important since condensable materials will accumulate on the cold detector surface. If too much contamination build-up takes place, e.g. ice in the early phases of the mission or possibly worse, hydrocarbons, the CCD bench can be heated-up, to boil-off contaminants.

3.3. Instrument Operating Modes

Three operating modes are available with the RGS: Spectroscopy, High Time Resolution and Diagnostic. Spectroscopy mode will presumably be the one most commonly used in flight as the baseline; the nine CCDs are read-out sequentially in frame transfer, with 3 x 3 on-chip binning (thus the pixel size becomes 81 micron, which still oversamples the RGS resolving power sufficiently). With a read-out time of 0.6 sec per CCD, the minimum accumulation time in Spectroscopy mode is 5.4 sec, if the nine CCDs are read-out continuously.

Several on-board processing options are available, such as selectable energy thresholds for noise reduction, selectable areas in the CCD image sections, split event reconstruction, single event selection and other types of data reduction to prevent telemetry overload.

The High Time Resolution (HTR) mode affords the shortest accumulation time, approximately 15 msec if only one CCD is read-out continuously. This is achieved by adopting a particular

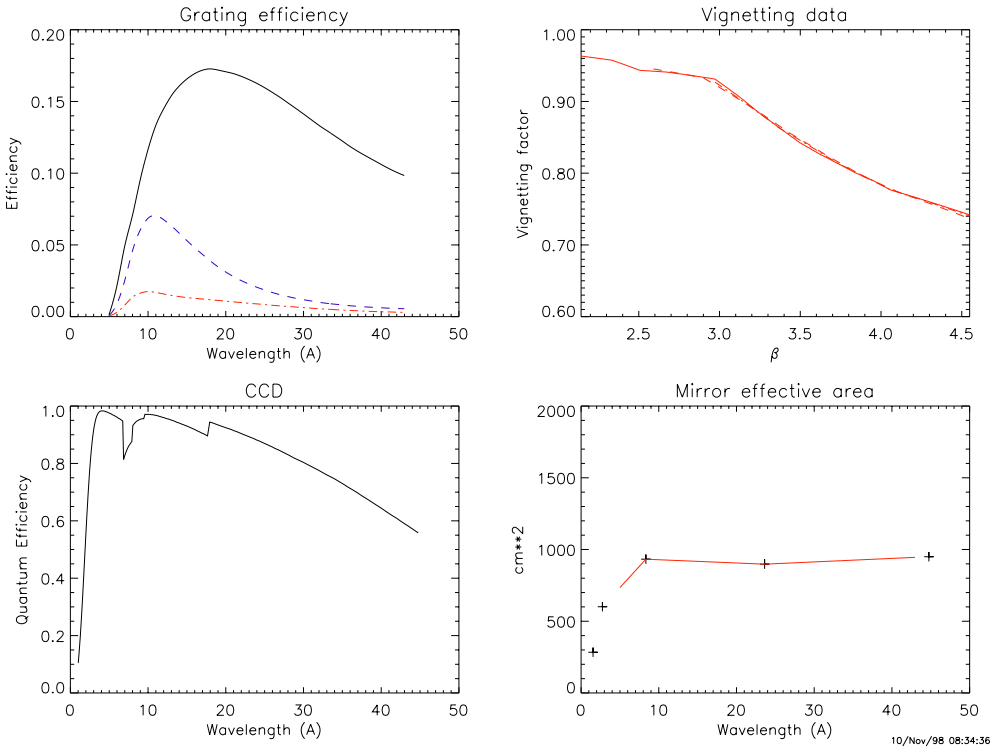

Fig. 6.— Calculated quantum efficiency and measured points as a function of wavelength of the strip of nine CCDs.

read-out technique whereby, after each accumulation, both the image and storage sections of the CCD undergo a 74 line shift, thus creating a stack of accumulated spectra over both the image and storage sections, and resulting in 74 line blocks being shifted into the read-out register every time. This register is then read-out without on-chip binning. More than one CCD can be used to collect data, but this increases the accumulation time.

The onboard processing described above can also be completely by-passed and all pixel data (including noise pixels) from one CCD read out can be transferred directly to a 'queue memory' which is part of the RGS digital electronics. These raw data, invaluable for dark current and system noise level determination, hot pixel verification, and troubleshooting, are subsequently telemetred to ground, either very quickly, in less than 1 min at 22 kbit/sec (in the so-call Diagnostic mode), or at a slower rate, interleaved with Spectroscopy data.

4. Predicted (model) and Measured Performance

4.1. Resolving power (of point sources).

Determining the resolving power $\lambda/\Delta\lambda$ or $E/\Delta E$ of the spectrometer involves modelling and measuring the line spread function (LSF) of the spectrometer in response to monochromatic radiation.

The RGS angular (or wavelength) response to monochromatic radiation has two distinct physical components. The core of the profile is determined by geometrical optics: the telescope angular response, the grating figures, the grating-to-grating alignment, and the focusing of the telescope. This core can be calculated reliably with a raytrace, based on an explicit model for the various components of the RGS. The parameters of this model have been calibrated in separate tests at sub-assembly level (telescope, RGA, individual gratings), and the resulting model has been validated in the end-to-end tests of both spectrometers at the Panter X-ray testing facility of the Max Planck Institut für Extraterrestrische Physik.

Microroughness on the gratings causes scattering of light, the amplitude and angular distribution of which scale completely different with wavelength and dispersion angle (or spectral order) from the core shape. A theoretical model for the redistribution of light due to the scattering was developed, based on first order perturbation theory scalar diffraction. The free parameters of this model, the r.m.s. amplitude and correlation length of the surface fluctuations, were calibrated on a subset of the gratings at Columbia, and the resulting scattering redistribution kernel was verified in the end-to-end tests at Panter.

The characteristic two-component shape of the resulting Line Spread Function (response integrated over the cross-dispersion direction) can be seen in Figure 7 (a,b) which shows the response of the RGS1 to Mg Kα radiation (λ9.89 Å) in spectral orders $m = -1, -2$, as measured at Panter. Overlaid on the data are the simulations calculated with the current best model for the instrument. The Mg K impact source emission spectrum is complex, and in addition to strong Mg Kα radiation also contains weaker subsidiary ('satellite') transitions at slightly higher energies, which are visible to the right of the Kα transition in Fig.7; they were not included in the response model. As is clear from these figures, the LSF can not adequately be represented by a single simple profile function (e.g. Gauss or Lorentzian), at least not at all wavelengths. Therefore, to characterize the resolving power of the RGS two separate measures are shown, one based on the HEW of the LSF, one based on the FWHM (Figures 8 (a-d)). Since the core shapes are slightly different for both spectrometers (due to different grating-to-grating alignment parameters), the resolving power is shown separately for both instruments. In order to assess whether two closely separated spectral lines can be resolved, the resolving power based on FWHM is the appropriate measure. To evaluate the detectability of a weak feature against a strong continuum, the resolving power based on HEW is the appropriate figure.

At long wavelengths, scattering is unimportant, and the LSF is dominated by the

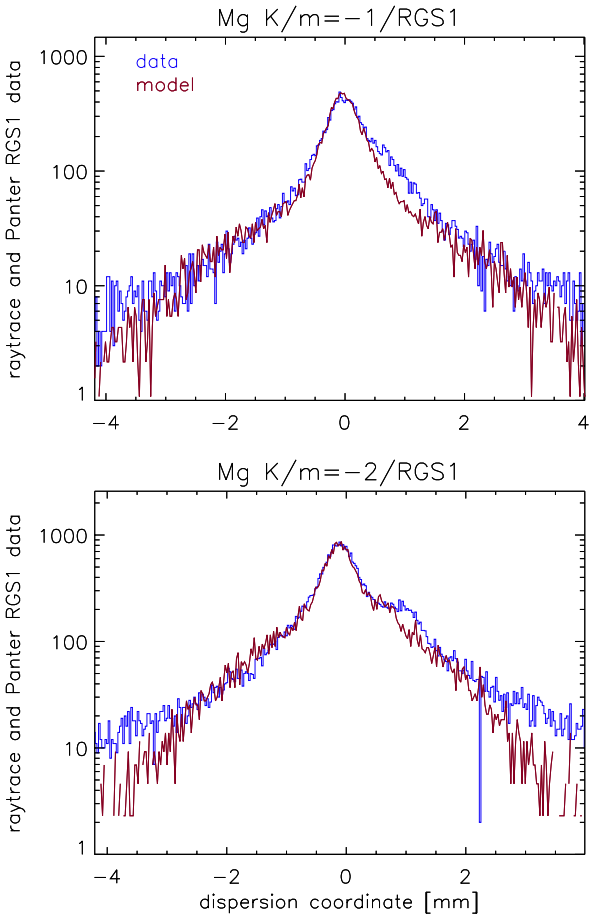

Fig. 7.— Measured (*blue*) and predicted (*red*) Line Spread Function at Mg K, for RGS1, in first and second order.

nearly-Gaussian core of the profile. The resolving power therefore asymptotically approaches approximately $R(\lambda/\Delta\lambda) \approx \text{constant} \cdot \lambda$, since $\Delta\lambda$ for the core is only a weak function of λ. At short wavelengths, scattering is relatively more important, and the resolving power curves decline faster than proportional to λ. The final modeling of the scattering behavior in this regime is still in the process of refinement, and the precise shape of the resolving power curves for wavelengths shorter than about 8 Å may therefore change somewhat with improved modeling.

The modeling of the scattering behavior and its effect on the Line Spread Function (resolution) and effective area, has been dealt with in two posters of J. Cottam et al and J. Spodek et al, this workshop.

Resolving power of extended sources.

The discussion above and the numbers quoted, apply to point sources. Extended sources, will be imaged in the cross-dispersion direction. In the dispersion direction, the extended image

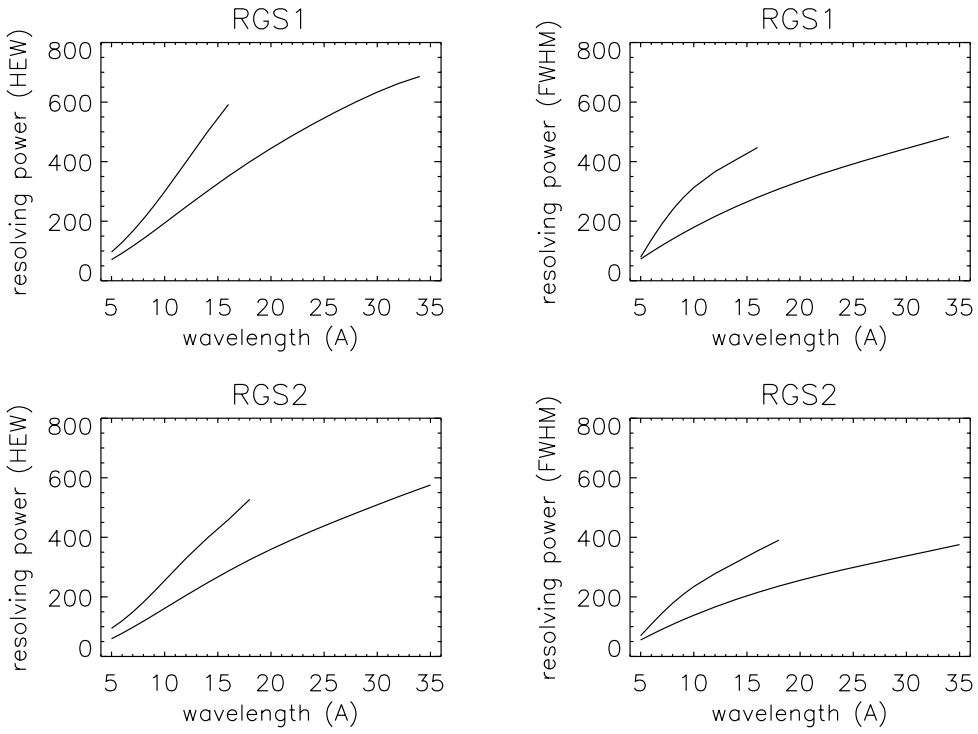

Fig. 8.— Predicted resolving power of the RGS, for RGS1 (*top*) and RGS2 (*bottom*); both the resolving power based on HEW (*left*), and FWHM (*right*) are given.

and spectral response are convolved. However, extended sources, small compared to the XMM telescope HEW of 15 arcsec, can be considered point sources of course. This in contrast to the grating spectrometers on AXAF, where the source extent has to be compared with the AXAF-HEW, which is of the order of one arcsecond. The additional contribution to the resolution, $\Delta\lambda_{ext}$ (in Å), for extended sources becomes $\Delta\lambda_{ext} = (0.124/m) \cdot \Delta\theta$, where $\Delta\theta$ is the source extent expressed as a one dimensional HEW in arcminutes and m is the diffraction order.

4.2. Effective area.

The effective area of three spectral orders $m = -1, m = -2$, and $m = -3$, for one RGS-instrument has been calculated and is shown in Figure 9. The total available area for observation is therefore twice this value. It includes, the telescope effective area, grating geometry (beam coverage), the grating efficiency, grating array internal vignetting, CCD-efficiency. All the different components have been calculated and measured separately, and the total system has been verified at Panter.

Also the telescope itself was calibrated at Panter. For the telescope tests and the comparison

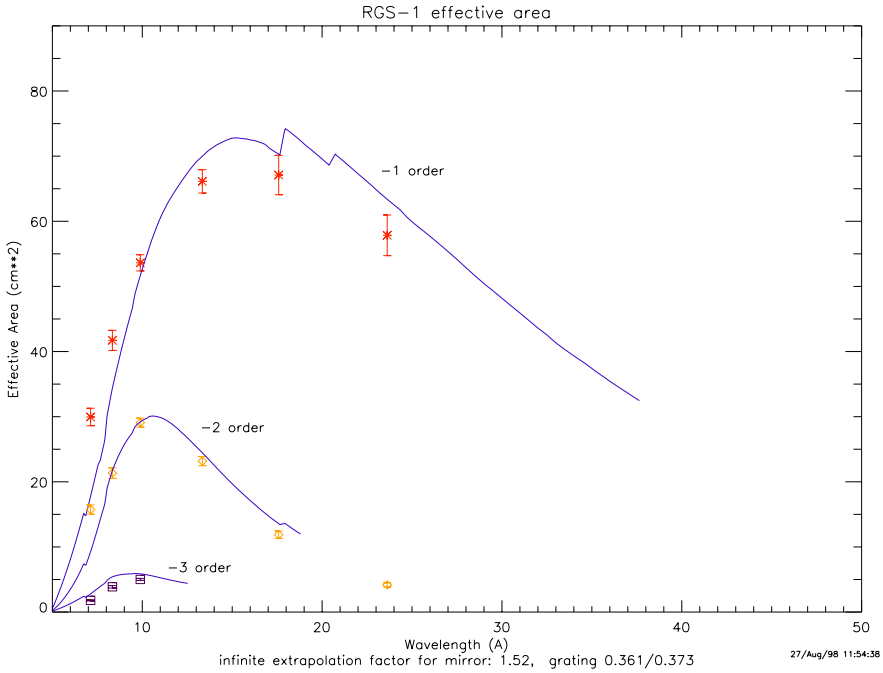

Fig. 9.— Effective area for *one* spectrometer; the solid curves are the current model prediction, the data points are measured effective area's obtained from RGS end-to-end ground calibrations by scaling the mirror throughput to flight efficiency.

between telescope area at Panter with finite source length and in-flight configuration, with parallel incidence beam, see Aschenbach et al, this workshop. The effective area curve in figure 9 applies to the in-orbit configuration. The measured points at the O-K, Fe-L, Cu-L, Mg-K, Al-K and Si-K are adjusted for the in-flight case. Comparison of effective area model and Panter measurements is still on-going. Particularly, one C-K data point (at 44 Å, slightly outside the nominal band) will confirm the long wave length tail. For a state of the art discussion on the effective area, see the poster by C. de Vries et al, this workshop.

5. Calibration measurement at Panter

As an example of what the raw data of RGS looks like and to discuss some of the specifics of the instrument, a measurement of the complete instrument at the Panter long beam X-ray test facility is presented in Fig. 10.

The panel shows a spectrum of an electron impact source with a macor target. (Macor is a machinable ceramic and contains Si, Al, Cu, Mg, Fe, O...). The spectrum consists of a continuum with lines in first, second and third spectral order. The dispersion runs along the horizontal axis, with the shortest wavelength (highest energy) at the right hand side. The vertical axis is the

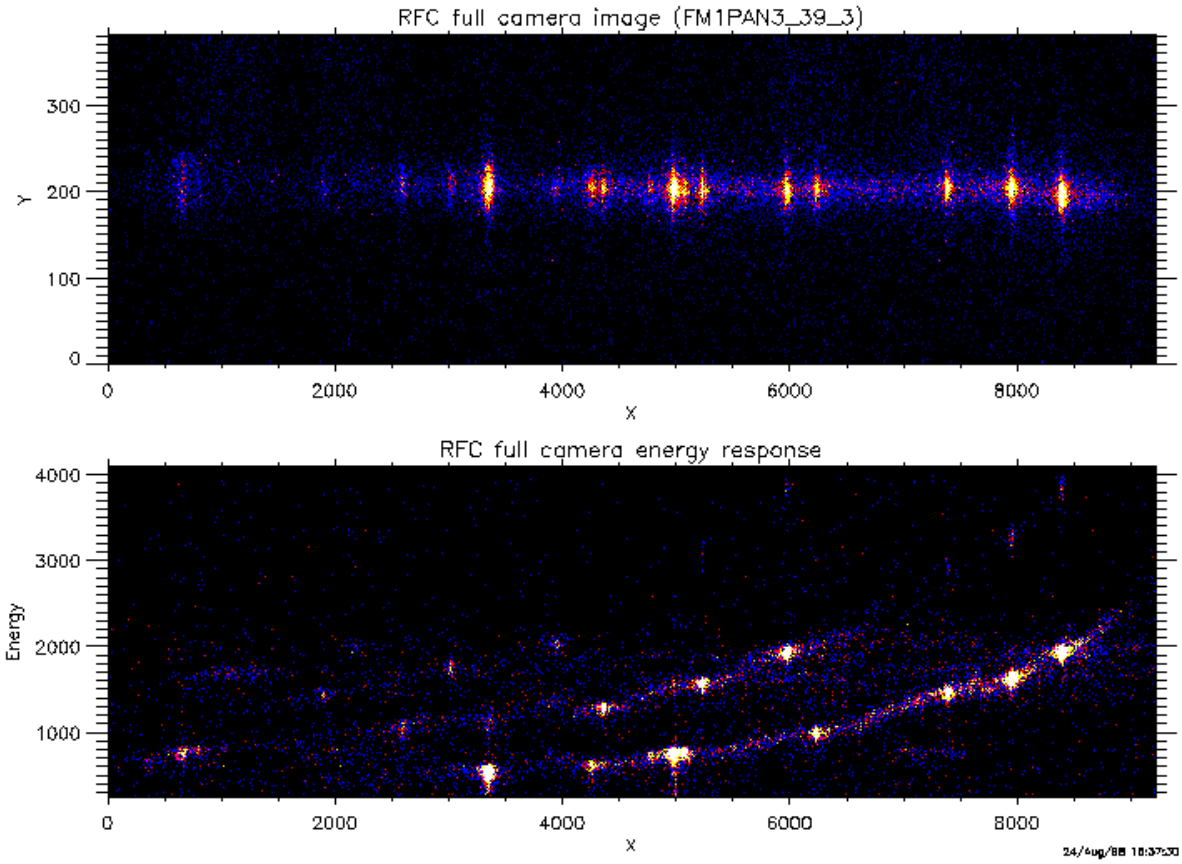

Fig. 10.— Raw calibration spectrum, obtained with RGS1 at Panter; X-ray source is a ceramic composite impact source. Top panel shows the two-dimensional spectral image, bottom panel shows the events represented in the CCD pulse height/dispersion plane (pulse height [in ADU] increases vertically between approximately 0 and 3700 eV; wavelength increases *approximately* linearly from right to left, between 5 and 35 Å (first order)).

cross-dispersion direction.

The bottom panel has again the dispersion direction along the horizontal axis and along the vertical axis is plotted the measured energy as seen by the CCD (the numbers along the vertical axis roughly equals eV). This plot represents raw data without any processing. At first glance the three spectral orders are nicely separated by the CCD intrinsic energy resolution. Closer examination reveals peculiarities that the data analysis software (and the observer) should be aware of.

As an example take the first order Si-K line, the bright dot at the right end, at about 2000 eV. Here exists a low level, a few percent, scattering component of Si-radiation as follows from the horizontal extent (photons with identical energy). Pile-up events can be seen at twice the

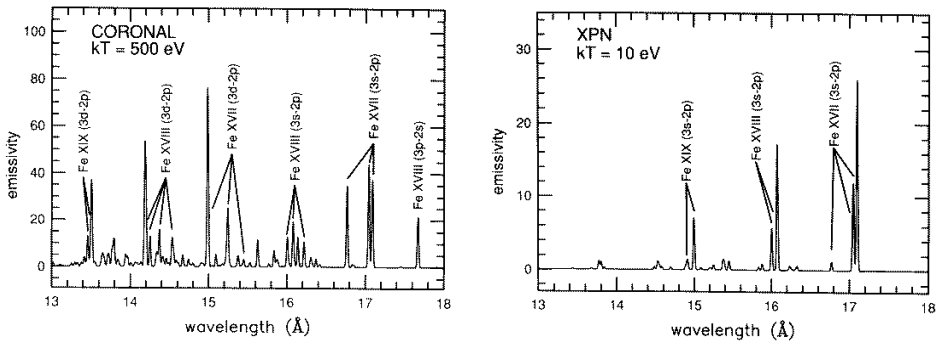

Fig. 11.— Emission line spectra from selected Fe L ions under conditions of collisional ionization equilibrium (*left*), and photoionization equilibrium (*right*) (from Liedahl *et al.* 1990).

energy of the lines. (Pile-up events occur when two photons are detected in one pixel during one accumulation period.) Contrary to imaging instruments, RGS will not suffer from pile-up while observing astrophysical sources, because the photons of a source are not focussed at one spot but dispersed over many pixels of course. At the position of strong lines one notices a vertical blurring towards lower energy, these are so-called partial events. Partial events are events caused by photons detected in the CCD, close to the surface, whereby part of the charge is lost. This is an energy dependent effect that plays a role at a few percent level. Furthermore the weak in-flight calibration sources (Al and F) can be seen at the predicted positions. Further careful inspection of the image shows small gaps between the CCDs, differences in gain between CCDs and CCD-halves (which shows up as small jumps in the vertical direction). All these effects were known and predicted and can now be verified and quantitatively accessed on system level. In a separate paper, A. Rasmussen et al, this workshop, a method for extracting the input spectrum from a similar data set is discussed. See also F. Paerels et al, this workshop.

6. Science with RGS

The study of Fe-L line complexes around 15 Å will be valuable to help reveal the underlying X-ray emission mechanism. This is clearly shown in Fig. 11, from Liedahl et al 1990, where a model spectrum of Fe XVI-XIX of a coronal spectrum is compared to a model spectrum of a photo-ionized spectrum with identical electron density. There is a marked difference between the line complexes which will allow to distinguish collisionally excited (coronal) from photo-ionized plasmas. See also F.Paerels, this workshop.

A new feature in non-solar X-ray astronomy will be the capability of electron density measurements with AXAF and XMM. Fig. 12 shows a simulation of the O VII triplet, using the

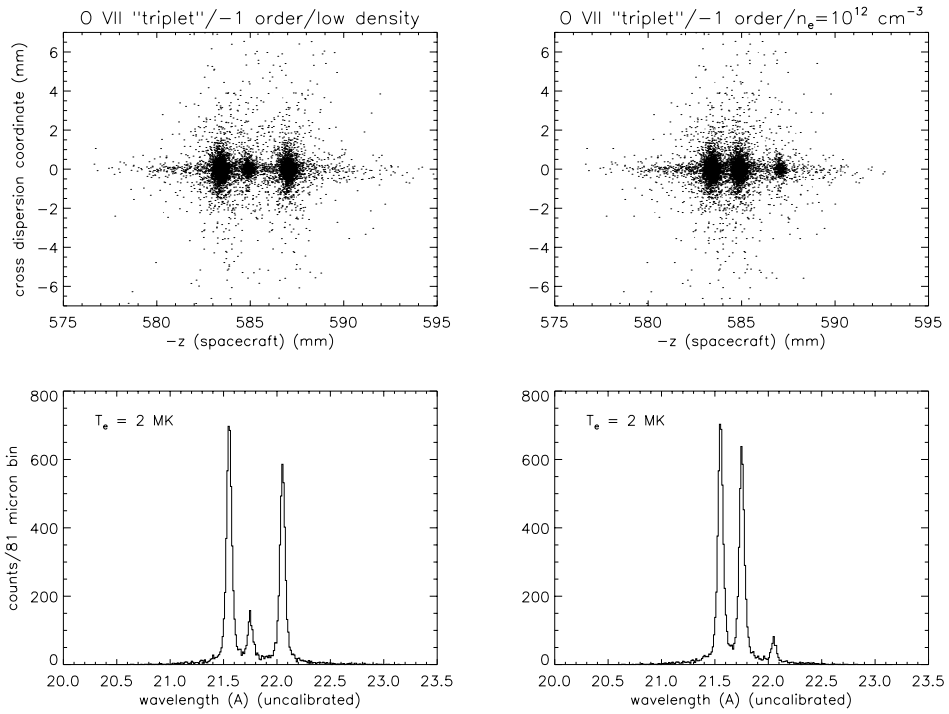

Fig. 12.— Explicit simulation of the O VII 'triplet' in the RGS (first order). Resonance, intercombination, and forbidden lines appear left to right. The top panels show spot diagrams (photon positions in $(-z, y)$ space), with dispersion increasing to the right. The lower panels show the corresponding histograms; the horizontal scales of top and bottom panels are matched. The left hand simulations were done at low density (well below the critical density of $n_{e,c} = 1.2 \times 10^{11}$ cm^{-3}), the right hand simulations were done above the critical density ($n_e = 1 \times 10^{12}$ cm^{-3}).

RGS resolving power and assuming a plasma temperature of 2 MK and two different electron densities, a low density case, $n_e \approx 10^{11}$ cm^{-3} (left panels) and a high density case, $n_e \approx 10^{12}$ cm^{-3}. The resonant line of the triplet (left one) remains constant, but the ratio between intercombination (middle) and a forbidden line (right) changes considerably. The resolving power of RGS is clearly sufficient to resolve the triplet and measure the ratio of intercombination and forbidden line quantitatively. (See also F. Paerels and references therein for discussion on line forming processes.) Not in all cases the triplets are so well resolved as follows from the simulation of Mg XI, see Fig. 13. Although with this first order spectrum, the ratio of intercombination and forbidden line intensity cannot quantitatively be established without some higher level analysis, the general shape of the partly resolved lines, will allow density estimates. In addition to the helium-like triplets, to diagnose plasma densities in the range 10^{10} to 10^{16} cm^{-3} and in the temperature range between 1.5 and 7 MK, the RGS band contains iron and nickel ions from a number of successive ionization stages, that can be applied for diagnosing plasmas in the density range $10^{10} - 10^{15}$ cm^{-3} and temperature range 5-15 MK (Mason 1984, Mewe 1985).

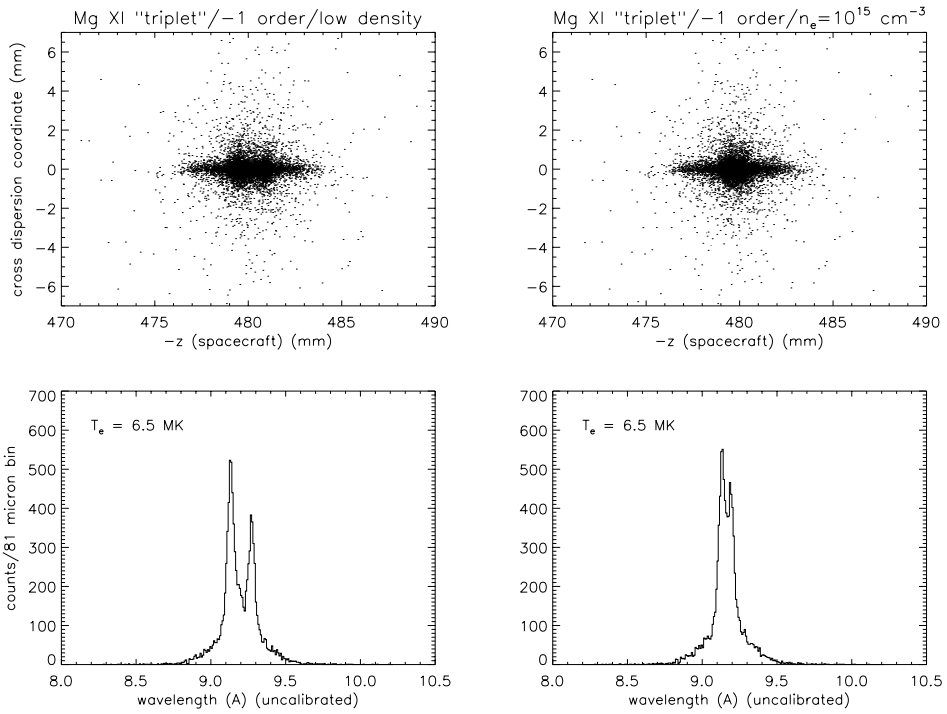

Fig. 13.— As Fig. 12, but for the Mg XI triplet; the critical density for Mg XI is $n_{e,c} = 4 \times 10^{13}$ cm^{-3}. The high-density simulation was done at $n_e = 1 \times 10^{15}$ cm^{-3}. The shift in balance between the forbidden and intercombination lines is clearly visible, going from low to high density; the extraction of quantitative density estimates from first order Mg XI images may require some 'deblending' analysis.

To show the potential of RGS, three different astrophysical objects have been simulated hereafter:

a) a coronal plasma, the example is Capella.

b) a supernova remnant in the large Magellanic Cloud, N 132D.

c) a Virgo-type cluster, at a large distance, 60 Mpc, simulating a small core with cool plasma embedded in a hot cloud. See figure captions for details.

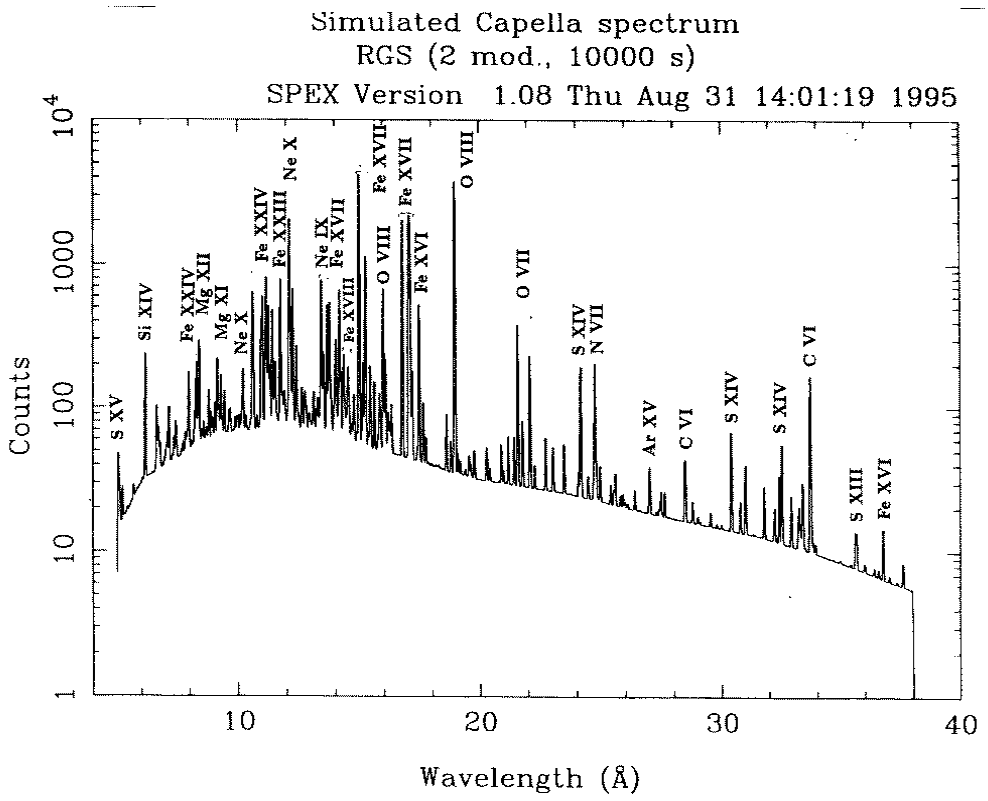

Fig. 14.— Simulated spectrum for Capella (two RGS modules added, 10000 sec exposure), assuming a collisional equilibrium plasma model. The emission measure distribution has been approximated by two discrete temperatures, kT = 0.4 and 2.2 keV, with emission measures 5×10^{52} and 1.5×10^{53} cm^{-3}, respectively. The power of X-ray spectroscopy with the RGS for diagnosing the physical conditions in stellar coronae is obvious from even a superficial inspection of the figure.

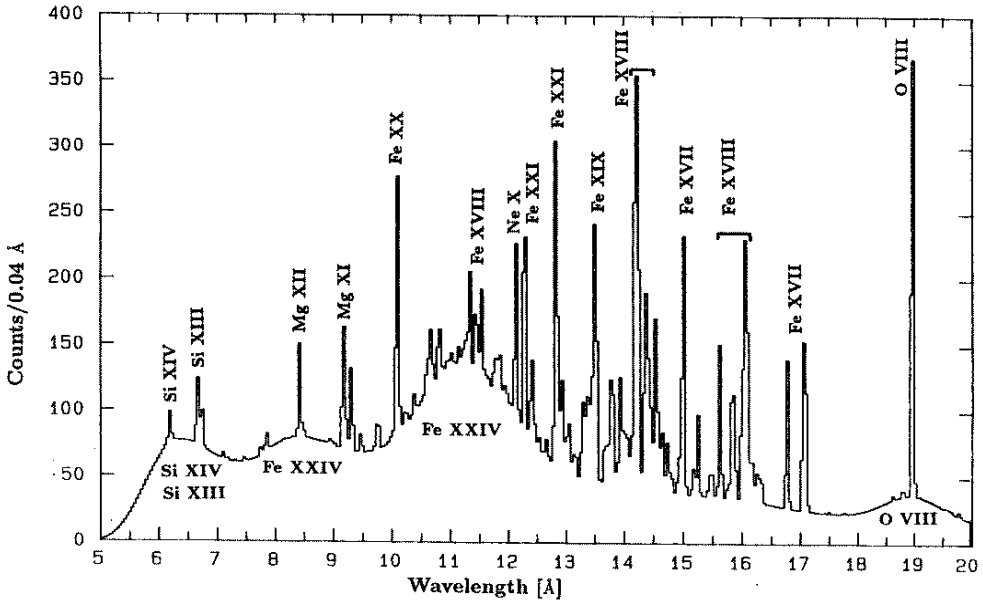

Fig. 15.— Simulated spectrum for a Virgo-like cluster, at a distance of 60 Mpc, for a 10^5 sec exposure (data from both spectrometers added). One sees the contribution from the extended, hot ($kT > 2$ keV) cluster 'atmosphere' as the broad, essentially unresolved component to the spectrum; superimposed is the emission from the bright, line-rich ($kT < 1$ keV) cooling flow, which, at a typical size of 2 arcmin, still produces a high resolution spectrum despite its finite extent.

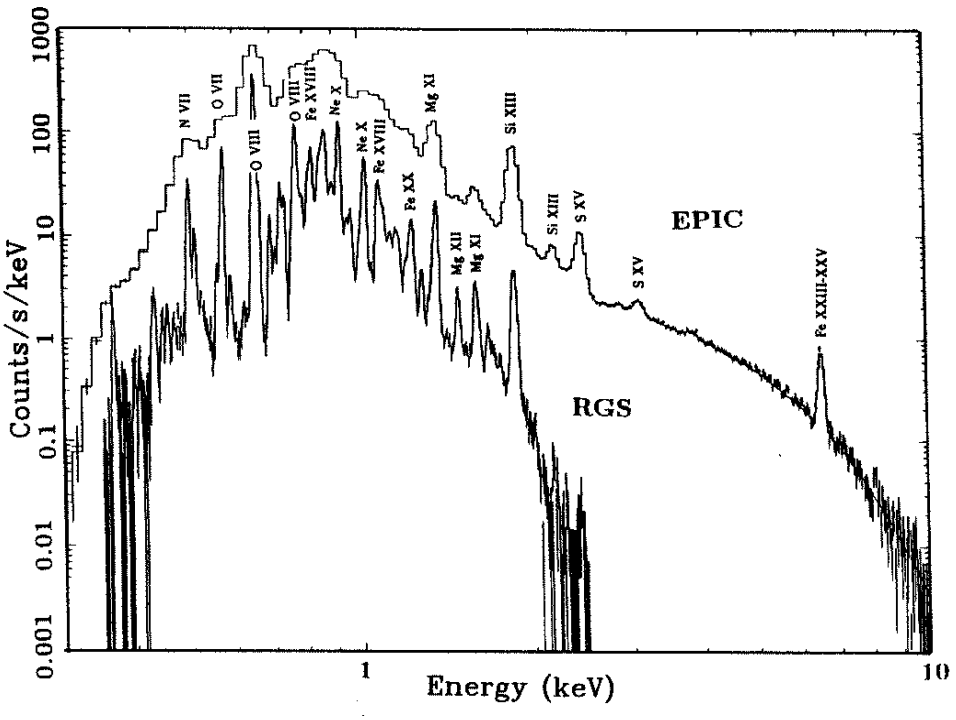

Fig. 16.— Simulated RGS and EPIC spectra for the bright LMC supernova remnant N132D (10^4 sec exposure). The smaller SNR in the LMC are ideal targets for the RGS—with its large dispersion, the RGS still produces a high resolution spectrum of the remnants despite their finite extent. This particular example shows that it will be possible, for instance, to spectroscopically diagnose non-equilibrium effects in the young remnants, and obtain correct abundance estimates. This simulation includes NEI effects, and assumed an abundance pattern appropriate to a type II SN.

REFERENCES

A.C. Brinkman, H.J.M. Aarts, G. Branduardi-Raymont, C.J. Hailey, F.A. Jansen, S.M. Kahn, P.A.J. de Korte, A. Zehnder, "Spectroscopic investigations with a reflection grating spectrometer", SPIE Vol. 1159, EUV, X-Ray, and Gamma-Ray Instrumentation for Astronomy and Atomic Physics, 495, (1989).

K. Thomsen and G. Heidenreich, "XMM-RGS Cryogenic Detector Housing", 24nd International Conference on Environmental Systems and 5th European Symposium on Space Environmental and Control Systems, Friedrichshafen, Germany, June 20–23, 1994.

K. Thomsen, "Compound Radiator" in Proceedings of the 4th European Symposium on Space Environmental and Control Systems, Florence, Italy, 21–24 October, 1991, (ESA SP 324, December 1991)

S.M. Kahn, T.A. Decker, J. Hailey, F.B.S. Paerels, S.M. Pratuch, A. Rasmussen, A.C. Brinkman, J.W. den Herder, "XMM reflection grating arrays", SPIE Vol. 2808, 1996.

T.M.V. Bootsma et al., "Back-illuminated CCDs as x-ray detector for the reflection grating spectrometer on-board XMM", SPIE Vol. 2808, 1996.

M.L. van den Berg, A.J.F. den Boggende, T.M.V. Bootsma, J.W. den Herder, F.A. Jansen, P.A.J. de Korte, E.J. van Zwet, T. Eaton and R. Ginige, "Back-illuminated CCDs made by Gas Immersion Laser Doping", NIM.-A, 1996, accepted for publication.

H.E. Mason, G.A. Doschek, K. Feldman and A.K. Bhalia, 1979, 73, 74.

R. Mewe, E. Gronenschild and G. van den Oord, 1985, A&AS, 62, 197.

D.A. Liedahl, S.M. Kahn, A.L. Osterheld and W.H. Goldstein, 1990, ApJ, 350, L37.

This preprint was prepared with the AAS LaTeX macros v4.0.